Planar Hall effect and magnetoresistance of Sb_2Te_3 epitaxial films

Ravinder Kumar,[1] Prabesh Bajracharya,[1] Paul Haghi Ashtiani,[1] Ryan Paxson,[2] Rajeswari Kolagani,[2] and Ramesh C. Budhani[1,*]

[1] *Department of Physics, Morgan State University, Baltimore, Maryland 21251, USA*
[2] *Department of Physics, Towson University, Towson, Maryland 21252, USA*

(Received 15 September 2023; accepted 29 January 2024; published 16 February 2024)

The measurements of anisotropic magnetoresistance (AMR), planar Hall effect (PHE) and temperature-dependent conductivity in materials with strong spin-orbit coupling yield valuable information about charge carrier scattering processes, localization effects, and band topology. Although electronic structure calculations establish the sesqui-chalcogenide Sb_2Te_3 a topological insulator (TI), detailed measurements of AMR and PHE are valuable to address the manifestations of the band topology on charge carrier transport in this system. Here, we report on measurements of the longitudinal and Hall resistivity, ρ_{xx} and ρ_{xy}, respectively, of the Sb_2Te_3 films of varied crystallinity over a wide phase space of temperature (T), magnetic field (**B**), and the angle between **B** and charge current density (**J**). The films exhibit semiconducting or metallic behavior depending on their crystallinity. The epitaxial films on (0001) sapphire grown at 150 °C are metallic with a hole carrier density (n_h) and mobility (μ_h) of $\sim 10^{19}$ cm^{-3} and $\sim 10^2$ cm^2 V^{-1} s^{-1}, respectively, at room temperature. The conduction in the semiconducting film exhibits a Shklovskii-Efros (SE)-type variable range hopping (VRH) at very low temperature, with a transition to the Mott type VRH at $T \geqslant 30$ K. The SE-type VRH is characterized by a Coulomb gap of 0.3 meV and a localization length of ≈12 nm, which matches with the average crystallite size in these disordered films. While signatures of weak antilocalization are seen in the magnetoresistance (MR) of epitaxial films at $T \leqslant 20$ K, the MR at $T > 20$ K agrees with Kohler's rule when corrected for the temperature variation of carrier density. The epitaxial films are characterized by a negative AMR and PHE which varies quadratically with magnetic field, but the orbital plots of ρ_{xy} vs ρ_{xx} negate the presence of a chiral anomaly in transport. The amplitude of MR anisotropy for 100 °C grown Sb_2Te_3 film is ≈ 102nΩm at 300 K, which is an order of magnitude larger than in Bi_2Te_3 and potentially important for the development of AMR-based sensors.

DOI: 10.1103/PhysRevB.109.075421

I. INTRODUCTION

The sesquichalcogenide Sb_2Te_3 is one of the best-known thermoelectric materials due to its relatively high figure of merit for thermoelectric power generation near room temperature (RT) [1–9]. Structurally, Sb_2Te_3 belongs to a family of layered compounds exhibiting the same tetradymite structure as of Bi_2Te_3, where the hexagonal quintuple layers of Sb (or Bi) and Te atoms are weakly bonded by van der Waals forces along the c-axis of the unit cell [10–12]. In general, Sb_2Te_3 shows p-type conductivity due to intrinsic defects such as antisites where Sb atoms occupy the lattice positions of tellurium. This leads to a high hole concentration of $\sim 10^{19}$ cm^{-3} [13]. In recent years, Sb_2Te_3 and Bi_2Te_3 have attracted much attention due to the nontrivial topology of their electronic bands [14–17]. Topological insulators (TIs) exhibit an insulating interior where only surface conduction is allowed, which is protected by time-reversal symmetry. These electronic attributes of the TIs are potential routes for realization of new quantum phenomena and quantum devices. However, the conducting surface states are very fragile, and their realization is possible mostly in defect-free single crystals and, to some degree, in epitaxial films in the regime where thin film size effects are not dominant. The band topology of Sb_2Te_3 has been addressed using angle-resolved photoemission spectroscopy measurements on single crystals [18,19] and thin epitaxial films [20,21]. Sb_2Te_3 is an extensively studied material in the bulk polycrystalline and textured thin film forms. These studies are targeted optimization of the thermoelectric power factor and figure of merit [1,2,5,10,22,23]. High-quality single crystals of pure and doped Sb_2Te_3 are primarily used for studies of quantum transport [2,24,25], whereas such studies on epitaxial films are sparse, but there are some reports on films grown by molecular beam epitaxy (MBE) [6,26–28], magnetron sputtering [22,29–31], and metal organic chemical vapor deposition (MOCVD) [32]. One important electron transport phenomenon that brings forth the contribution of nontrivial topology of electronic states near the Fermi energy to electrical conductivity is anisotropic magnetoresistance (AMR) and the concomitant planar Hall effect (PHE). While AMR and PHE have been discussed theoretically in the framework of a nonvanishing Berry curvature of states [33], experimental data are desired to address the predictions of the theory.

Here, we report on the measurements of orbital magnetoresistance (OMR), Hall resistivity, AMR, and PHE on thin films of Sb_2Te_3 grown at various temperatures using the pulsed

*ramesh.budhani@morgan.edu

 ©2024 American Physical Society

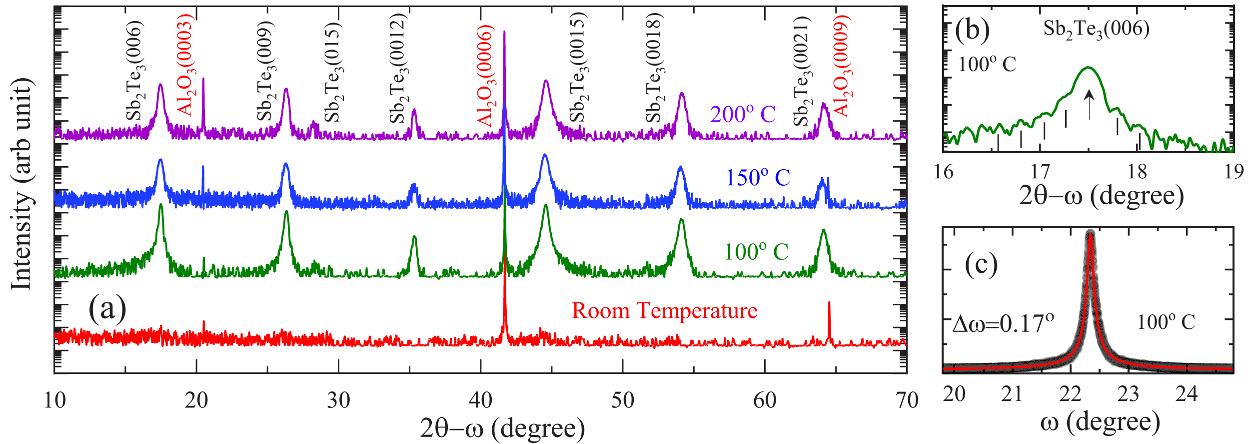

FIG. 1. Results of x-ray diffraction measurements on Sb_2Te_3 films performed using Rigaku smart lab setup. (a) 2θ-ω scans of ≈160-nm-thick films grown at room temperature, 100, 150, and 200 °C on *c*-plane sapphire. (b) The Laue oscillations seen in the vicinity of the (006) reflection of the 100 °C grown film. (c) Rocking curve measurement on the 100 °C grown sample.

laser deposition (PLD) method. The crystallographic structure of these films varies from epitaxial to noncrystalline depending on the temperature of growth. The magnetotransport measurements performed in the temperature and magnetic field ranges of 2 to 300 K and 0 to ±9 T, respectively, establish the nature of charge carriers and their mobility. High-resolution electron microscopy of the disordered films display a granular structure, which leads to a Shklovskii-Efros (SE)-type [34–38] hopping conduction at low temperatures. While the magnetoconductance measurements at small fields ($\leqslant$1 T) on epitaxial films display weak antilocalization (WAL) effects, the conductivity at high field follows a scaling behavior consistent with the modified Kohler's rule [39]. More interestingly, AMR and PHE of this nonmagnetic compound are negative and large ($\approx -102\,\mathrm{n\Omega m}$). These results have been discussed in the framework of the existing models of electronic transport in topological materials.

II. EXPERIMENTAL METHODS

The Sb_2Te_3 thin films were deposited on *c*-plane sapphire substrates using a pulsed KrF excimer laser ($\lambda = 248$ nm)-based PLD technique. A ≈100% dense melt-grown target of Sb_2Te_3 (elemental purity 99.999%) was ablated at the pulse repetition frequency of 5 Hz and areal energy density per pulse of $\approx 4\,\mathrm{J/cm^2}$ to yield a growth rate of 0.27 nm/s in ≈80 mTorr background pressure of ultrahigh purity argon. Optimal utilization of the target and uniformity of the growing film were ensured by rotating the substrate and rastering the laser beam on the surface of the rotating target. The films were deposited at 25, 100, 150, and 200 °C. We have also attempted to grow these films at $T \geqslant 250\,^\circ$C. However, the sticking coefficient of Sb and Te is nearly zero at these temperatures. The crystallographic structure, elemental concentration, grain size, and surface roughness of the films were characterized using a combination of transmission electron microscopy (TEM), energy dispersive x-ray microanalysis, x-ray diffraction, and x-ray reflectivity measurements. Electronic transport measurements were performed in a physical properties measurement system equipped with a 9 T superconducting magnet and a sample rotation arrangement to allow variation of the polar (θ) and azimuthal (ϕ) angles between the magnetic field and transport current. Samples for these measurements were patterned in the form of Hall bars.

III. RESULTS AND DISCUSSION

A. Structural characterization

Figure 1(a) shows several 2θ-ω x-ray diffraction patterns and ω scans performed on ≈160-nm-thick Sb_2Te_3 films grown on *c*-plane sapphire. While the diffraction profiles of the samples grown at RT (≈25 °C) shows no discernible peaks of Sb_2Te_3, suggesting a noncrystalline structure, the patterns of the films grown at 100, 150, and 200 °C exhibit strong Bragg reflections corresponding only to the (00l) reflections of the rhombohedral structure of Sb_2Te_3, indicating epitaxial growth. The *c*-axis lattice parameters calculated from the diffraction profile of the 100, 150, and 200 °C grown samples is 29.10, 30.49, and 30.46 Å, respectively, as compared with the bulk value of ≈ 31.78 Å. Since the in-plane lattice parameter a ($= b \approx 4.81$ Å) of the sapphire substrate is relatively larger than that of Sb_2Te_3, i.e., a ($= b \approx 4.30$ Å), it presumably leads to the observed out-of-plane *c*-axis compression. We observed prominent Laue oscillations of the intense Bragg reflections. Figure 1(b) shows such satellite reflections corresponding to the (006) Bragg peak. The presence of these oscillations in the diffraction pattern suggests a reasonably good epitaxial growth. Further, we performed rocking curve measurements around the most intense (0015) reflection. A representative rocking curve for 100 °C film is shown in Fig. 1(c). We estimate the full width at half maximum (FWHM) of the rocking curves measured for the 100, 150, and 200 °C grown films as ≈ 0.17°, 0.19°, and ≈ 0.16°, respectively. Although to the best of our knowledge no such measurements have been reported for PLD grown Sb_2Te_3 films, these values are comparable with the values reported for PLD grown Bi_2Te_3 [40]. The crystallographic structure of the RT grown samples has been investigated with TEM measurements as well to correlate it with electronic transport. Figure S1 in the Supplemental Material [41] shows a TEM

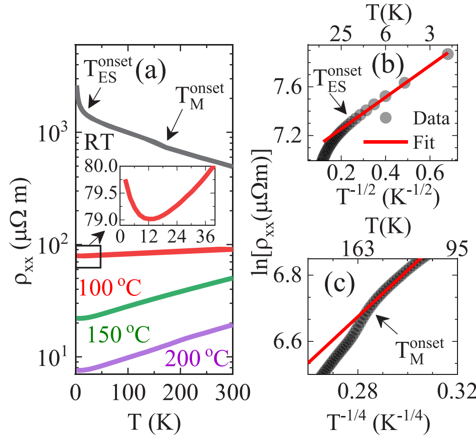

FIG. 2. (a) The temperature dependence of the zero-field longitudinal resistivity (ρ_{xx}) of the Sb_2Te_3 films grown at several temperatures. (b) The room-temperature (RT) grown sample follows the natural log resistivity vs $T^{-1/2}$ for the low-temperature regime, whereas it follows (c) natural log resistivity vs $T^{-1/4}$ for the high-temperature regime. Inset of (a) shows a magnified view of ρ_{xx} for 100 °C film to highlight weak localization effects at low temperature.

micrograph and the corresponding selected area diffraction pattern of a film deposited at 25 °C. The TEM data reveal that these films are not homogeneously amorphous but consist of nanocrystallites embedded in a disordered background.

B. Electrical resistivity and Hall mobility

The zero-field longitudinal resistivity (ρ_{xx}) of the films has been measured over a temperature range of 2 to 300 K. The ρ_{xx} (T) data for the films grown at RT, 100, 150, and 200 °C are shown in Fig. 2. The resistivity of the RT grown film exhibits a semiconducting behavior but without a uniquely defined activation energy, which suggests a carrier hopping dominated transport. On the contrary, the films deposited at 150 and 200 °C show metallic conduction with residual resistivity ratio (RRR) values of 2.3 and 2.5, respectively, which are smaller than the reported numbers for single crystals [11,42] and epitaxial films grown using MOCVD [20,32] but comparable with MBE grown films [26] and better than the values reported for polycrystalline Sb_2Te_3 [10]. The sample grown at 100 °C shows a drop in the resistance as the temperature decreases from 300 to 2 K, but the RRR is very low (∼1.1). We see drop in the mobility as a function of increment in the temperature, suggesting nonmetallic behavior, discussed in the upcoming sections. Further, the ρ_{xx} (T) data show a smooth variation with temperature, suggesting the absence of any phase or structural transition. The temperature-dependent resistivity of the RT grown samples is addressed in the framework of the hopping transport of charge carriers in disordered systems. The resistivity due to hopping conduction is expressed as [34–36,43]

$$\rho(T) \approx \rho_0 \exp\left[\frac{T_0}{T}\right]^{1/p}, \qquad (1)$$

where ρ_0 is a constant pre-exponential factor and T_0 is a characteristic temperature scale which depends on the material parameters such as the density of states (DOS) at the Fermi energy (E_F), extent of localized wave function, and the static dielectric function. For a three-dimensional (3D) system, the parameter p is equal to 1, 2, or 4 depending on the nature of hopping transport [34–36]. The exponent p is equal to 1 for the nearest-neighbor hopping conduction. The Mott formula with $p = 4$ is applicable for variable range hopping (VRH) in the localized state at the Fermi energy (E_F) [43]. In contrast, $p = 2$ corresponds to the opening of a SE-type Coulomb gap in the localized states at E_F. The applicability of these models of conduction depends on the extent of disorder in the system. When the disorder is weak and the charge carriers possess sufficient energy to overcome the Coulomb gap in the DOS at E_F, the Mott-type VRH is the mode of conduction. However, at sufficiently low temperatures, where the charge carriers may not have sufficient energy to cross the Coulomb gap, one sees the SE hopping. Between these two cases, some systems with intermediate disorder show a transition from SE to Mott types of VRH on going from low to high temperature [36]. The signature of electronic transport described by Eq. (1) is also seen in systems consisting of a fractal network on metallic islands separated by thin insulating barriers [38], and in thin films of 3D TIs like $(Bi_xSb_{1-x})_2Te_3$ containing charged defects induced by antisite disorder and magnetic dopants [37].

In Fig. 2(b), we show the variation of $\ln[\rho_{xx}(T)]$ in the low-temperature regime (2 to ≈30 K) as a function of $T^{-1/2}$. A constant slope of this plot supports the SE-VRH model of conduction. However, the data above ≈30 K, as shown in Fig. 2(c), are in better agreement with the $T^{-1/4}$-type dependence, indicating a dominant role of Mott VRH. The Mott VRH finally gives way to the nearest-neighbor hopping transport at $T \geqslant 141$ K corresponding to exponent $p = 1$. The characteristic temperature T_0 described in Eq. (1) can be used to calculate the localization length ξ of the charge carriers [44]:

$$\xi = \frac{\beta_2 e^2}{4\pi\varepsilon\varepsilon_0 T_0 k_B}, \qquad (2)$$

where $\beta_2(= 2.8)$, e, ε, ε_0, and k_B are numerical constant, electronic charge, dielectric constant, vacuum permeability, and Boltzmann constant, respectively. The static dielectric function ε for the disordered films of Sb_2Te_3 is ≈ 2200 [45]. With the value of $T_0 \approx 1.72$ K calculated from the slope of $\ln[\rho_{xx}]$ vs $T^{-1/2}$ plot [shown in Fig. 2(b)], the localization length comes out to be ≈ 12 nm. In the framework of the theory of electronic transport in 3D TIs, this length scale could be identified with the extent of charged puddles [36]. Since the system under consideration is not a homogeneously disordered material like the doped or amorphous Si or Ge, it is important to investigate the localization length of ≈12 nm in light of the microstructure of these films. Figure S1 in the Supplemental Material [41] shows a high-resolution transmission electron micrograph of the RT deposited Sb_2Te_3 sample. The presence of islandlike features of dimension ≈14 ± 2 nm in the micrograph with a crystalline interior, as evident from faint lattice fringes and the fine structure of the diffused diffraction rings, indicates that the low-temperature transport is controlled by tunnelling of charge carriers between these islands. The Coulomb gap

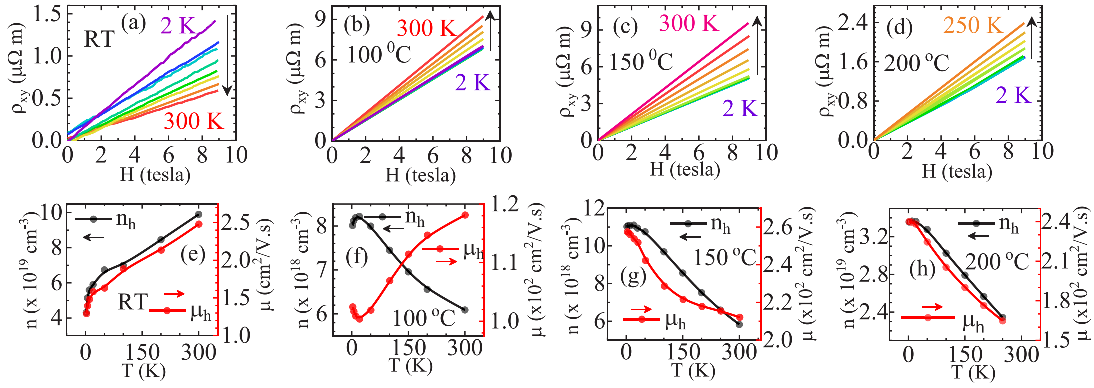

FIG. 3. Hall resistivity is plotted as a function of magnetic field at various temperatures for the films grown at (a) room temperature (RT), (b) 100 °C, (c) 150 °C, and (d) 200 °C. (e)–(h) show the carrier concentration and Hall mobility calculated from the ρ_{xx} and ρ_{xy} data plotted as a function of temperature for films deposited at RT, 100, 150, and 200 °C, respectively.

($\Delta_{\rm CG}$) associated with the SE conduction is expressed as [46]

$$\Delta_{\rm CG} = \frac{k_B}{2}\sqrt{T_0 T_{\rm ES}^{\rm onset}}, \tag{3}$$

where $T_{\rm ES}^{\rm onset}$ is the temperature of onset of the SE conduction on cooling the sample, which in this case is ≈30 K. With a T_0 of 1.72 K, $\Delta_{\rm CG}$ comes out to be ≈ 0.3 meV. In general, the Coulomb gap at the Fermi energy is a consequence of interactions between localized electrons in a disordered system [47]. In a narrow band gap semiconductor like Sb_2Te_3 containing a high-conductivity island randomly distributed over a poorly conducting background, the island may acquire a fractional charge from the impurities in the system. These fractionally charged islands create a random potential and hence the localization of electronic state and eventually a soft gap at E_F at sufficiently low temperatures [47,48]. It is expressed as $\Delta \approx [e^3 N^{1/2}(E_F)/\varepsilon^{3/2}]$, where e, $N(E_F)$, and ε are electronic charge, DOS at E_F, and static dielectric function, respectively [46]. Although the DOS in Sb_2Te_3 is in the range of 10^{19} to 10^{20} (states/eV cm^3), the large dielectric function (≈2200) of this material leads to a small (≈0.3 meV) Coulomb gap. However, this number is comparable with the Coulomb gap measured in Ge-Sn alloys [36,49] and $CuGaSe_2$ crystals [46].

At higher temperatures, when the carriers acquire sufficient energy, the electronic transport is not inhibited by the SE gap. A crossover between two different temperature-activated behaviors is seen in VRH. Generally, VRH evolves from the Mott regime with a $T^{-1/4}$ dependence at higher temperature to the SE with a $T^{-1/2}$ dependence when the temperature is lower than the width of the Coulomb gap [43,50]. The resistivity data shown in Fig. 2(c) clearly suggest a dependence of the type $\rho(T) \sim \exp{(T_m/T)^{1/4}}$, where T_m is the characteristic Mott temperature, which yields the localization length $\xi_M = (21 \pm 1)/[k_B T_M N(E_F)]^{1/3}$ [46]. However, an estimation of ξ_M requires the DOS at the Fermi energy. By approximating the DOS from the carrier density at ambient temperature [46], the localization length is ≈40 nm, which for a carrier density of 8×10^{18}/cm^3 comes out to ≈$\frac{1}{12}$ of the average distance between the carriers.

The results of the Hall resistivity measurements on the Sb_2Te_3 films as a function of magnetic field at various temperatures ranging from 2 to 300 K are shown in Figs. 3(a)–3(d). These are the antisymmetrized Hall resistivity data [$\rho_{xy}(B)$], where the contribution of a small unbalanced zero-field signal has been removed by using the expression $[\rho_{xy}(+B) - \rho_{xy}(-B)]/2$. Considering the dominantly linear field dependence of $\rho_{xy}(B)$ at all temperatures, these data have been analyzed in the framework of a single-band conduction model. The positive sign of ρ_{xy} in all samples indicates that holes are the majority charge carriers. A linear fit to the magnetic field dependence of ρ_{xy} yields the Hall coefficient (R_H), which is used to estimate the carrier concentration (n_h) and the Hall mobility (μ_h) by utilizing the expressions $n_h = 1/eR_H$ and $\mu_h = R_H/\rho_{(B=0)}$, respectively. The temperature dependences of n_h and μ_h for the RT, 100, 150, and 200 °C grown samples are shown in Figs. 3(e)–3(h), respectively. The carrier concentration at 300 K is the lowest (∼6.0×10^{18} cm^{-3}) for the films grown at 100 and 150 °C. However, for the films grown at RT and 200 °C, the ambient temperature value of n_h is ∼1.0×10^{20} cm^{-3} and ∼2.4×10^{19} cm^{-3}, respectively. The temperature dependences of n_h and μ_h of the RT and 100 °C grown samples also show a rapid variation between 2 to ≈20 K, like the dependence to the longitudinal resistivity where it is dominated by the SE hopping conduction. If we look at the temperature dependence of longitudinal resistivity of the 100 °C grown sample, even though the resistance decreases as the temperature is lowered from 300 to 2 K, the change is very small [$\rho_{xx}(300\,{\rm K})/\rho_{xx}(2\,{\rm K}) \approx 1.1$]. The carrier mobility shows a small (≈15%) increase with temperature. This type of temperature dependence of Hall mobility is expected when there is a change from band conduction to VRH at low temperature in the impurity band. A similar behavior of Hall mobility is seen in crystals of $CuGaSe_2$ [51]. However, a detailed understanding of the Hall conductivity in the hopping regime required modeling of the self-interference effects of the charge carrier wave function as it propagates along different hopping paths in a magnetic field [52,53].

The n_h and μ_h of the samples grown at 150 and 200 °C both show a decreasing trend as the temperature is raised from 2 K. The behaviors of n_h and μ_h measured at 2 and 300 K as a function of film growth temperature are shown in Fig. 4. It is interesting to note that the disordered film grown at RT exhibits a higher carrier concentration than all the crystalline films, whereas the Hall mobility is the least in this case.

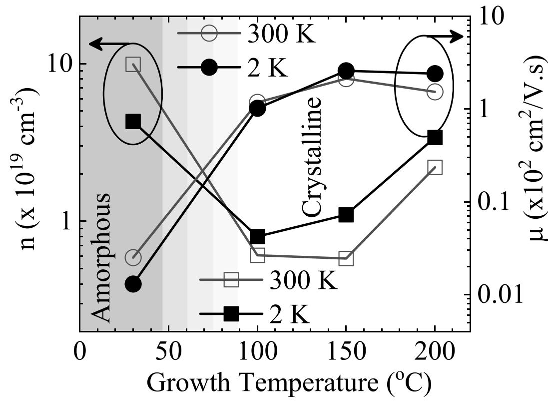

FIG. 4. The carrier concentration and Hall mobility at 2 and 300 K as a function of growth temperature. The shaded bands from the left to right in the figure represent increasing crystallinity. Samples grown at $T \geqslant 100\,^{\circ}$C are epitaxial.

The microstructure of the RT grown sample is very different. In this case, transmission electron micrographs show island like features embedded in an amorphous background (Fig. S1 in the Supplemental Material [41]). This indicates that the transport is controlled by tunnelling of charge carriers between these islands. Similar values of n_h (9.1×10^{19} cm^{-3}) and μ_h (20 cm^2/Vs) have been observed for a poorly crystalline film of Sb_2Te_3 [31]. The higher carrier mobility in the films grown at $T \geqslant 100\,^{\circ}$C is indicative of their (00l)-oriented epitaxial nature where the transport takes place in the conducting *ab* planes of the crystal. A sudden increase in the carrier concentration when the growth temperature exceeds 150 °C is suggestive of a tellurium (Te) deficiency in the film. Since the vapor pressure of Te at ∼200 °C is an order of magnitude higher than the vapor pressure of Sb, it is likely that the films become increasingly Te deficient as the growth temperature is increased. The consequences of high vapor pressure are seen dramatically when the growth temperature is increased beyond ≈ 300°C, where the sticking coefficients of Te and Sb approach zero and no film grows on the substrate. A similar dependence of n_h on the growth temperature has been reported by Fang *et al.* [29] for RF magnetron sputtered Sb_2Te_3 deposited on Si(100) substrates. Nonetheless, our results of n_h and μ_h for the 100 and 150 °C films are comparable with the results of a 400-nm-thick film of Sb_2Te_3 grown at 250 °C by MBE where the values of n_h and μ_h are $\sim9.13\times10^{18}$ cm^{-3} and $\sim7.81\times10^2$ cm^2/Vs, respectively [12]. Zhang *et al.* [28] report similar values of n_h ($\sim2.1\times10^{19}$ cm^{-3}) and μ_h ($\sim3.0\times10^2$ cm^2/Vs) for highly (00l)-textured Sb_2Te_3 grown by MBE on Si(111) at 280 °C. Kim *et al.* [6] show the range of variation of n_h ($\sim10^{19}$ to 10^{20} cm^{-3}) and μ_h ($\sim0.5\times10^2$ to 3.0×10^2 cm^2/Vs) for MBE grown films by varying the Te/Sb flux ratio.

C. Magnetoresistance

Together with the Hall measurements, we have also measured the out-of-plane magnetic field dependence of the longitudinal resistivity ρ_{xx}. Figure 5 shows the symmetrized $\rho_{xx}(B)$ $\{=[\rho_{xx}(+B)+\rho_{xx}(-B)]/2\}$ data measured at various temperatures. The RT grown sample shows a magnetoresistance (MR) ($=\{[\rho_{xx}(B)+\rho_{xx}(0)]/\rho_{xx}(0)\}\times100\%$) as large as ∼14% at 2 K, which drops rapidly on increasing the temperature [Fig. 5(a)], reaching a value of ∼0.2% at 300 K. The 100 °C grown sample has the smallest MR of ∼3% at 2 K, which drops to ∼1% at 300 K [Fig. 5(b)]. These numbers increase in films deposited at 150 and 200 °C, as seen in Figs. 5(c) and 5(d). The field and temperature dependences of MR in a broad class of materials including metals, doped oxides, semiconductors, and topological materials have been understood in the framework of Kohler's rule [39], which in its simplest form states that the MR should follow a scaling law of the form MR $= f(B/\rho_0)$, where B is the applied magnetic field and ρ_0 the zero-field resistivity at a given temperature. The scaling law predicts that all MR curves measured at different temperatures should fall into a single universal curve.

The MR of the samples grown at 25, 100, 150, and 200 °C is plotted as a function of B/ρ_0 in Fig. 5(e) and 5(f),

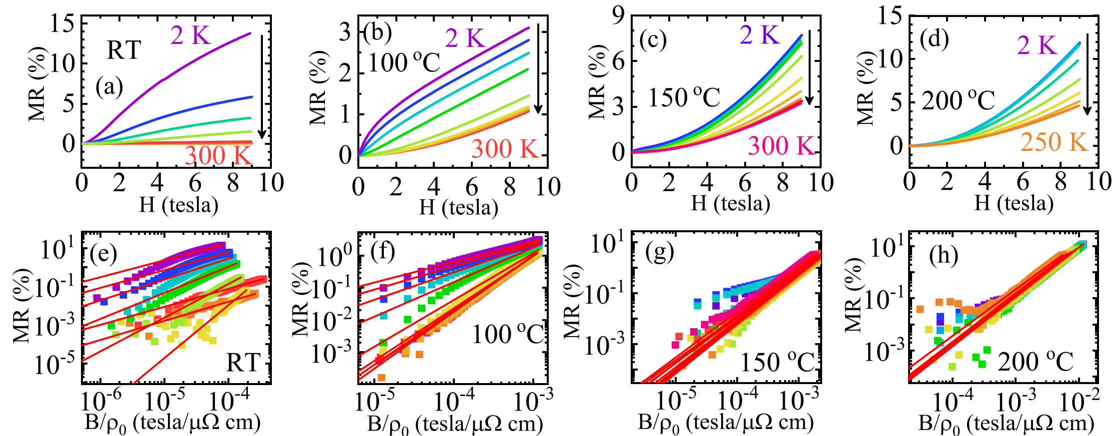

FIG. 5. Magnetoresistance (MR) measured as a function of magnetic field at various temperatures on (a) room temperature (RT), (b) 100 °C, (c) 150 °C, and (d) 200 °C grown samples. MR as a function of B/ρ_0 at various temperatures for (e) RT, (f) 100 °C, (g) 150 °C, and (h) 200 °C, and their corresponding Kohler's fitting is shown by red curve.

respectively. The MR of the disordered sample grown at 25 °C deviates strongly from the prediction of Kohler's rule. However, this is expected since, in the disordered state, the Boltzmann semiclassical transport theory, based on which Kohler's rule is derived, is not applicable. While we also observe deviations in the case of the crystalline samples grown at 100, 150, and 200 °C, these deviations clearly reduce as we increase the growth temperature. For example, in the case of the 150 °C grown sample [Fig. 5(g)], the overlap is only over the B/ρ_0 range of $\sim 6\times10^{-4}$ to $\sim 5\times10^{-3}$ $(\mathrm{T}-\mu\Omega^{-1}\,\mathrm{cm}^{-1})$, but for the 200 °C films, it extends from $\sim 5\times10^{-4}$ to $\sim 1\times10^{-2}$ $(\mathrm{T}-\mu\Omega^{-1}\,\mathrm{cm}^{-1})$. A modified form of Kohler's rule has been proposed by Xu *et al.* [39] to account for the temperature-dependent variations in ρ_0. The modified rule is expressed as $\mathrm{MR} = f[B/n_T\rho_0\ ]$, where n_T could be argued to be the carrier density renormalized by the carrier effective mass m^*. It successfully explains the MR of a class of nonmagnetic Weyl semimetals like TaP and the narrow band gap semiconductor InSb. We have applied the modified Kohler's rule propounded by Xu *et al.* [39] to the data of the epitaxial films grown at 150 and 200 °C, by using the carrier density (n_h) calculated from the Hall data. Here, we implicitly assume that the carrier mass remains temperature independent, and single-band model correctly describes the carrier transport in Sb_2Te_3. This modification results in a significant convergence of the data, as shown in Fig. S2 in the Supplemental Material [41]. In general, it has been observed that the validation/violation of Kohler's rule depends on the electron density in the limit of zero temperature [39,54,55]. The rule does not hold if the electron density is low, but it applies when the carrier density is high enough so that the thermally induced charges in its value are insignificant. The conventional metals and type-II Weyl semimetals with high electron densities of $\approx 10^{22}$–10^{23} cm^{-3} and high Fermi energies of a few electronvolts obey Kohler's rule. However, the type-I semimetals typically having low carrier densities fail to hold Kohler's law [39].

A noticeable feature of the MR in epitaxial films of Sb_2Te_3 is its field dependence at different temperatures. The MR of the 100 °C grown film at 2 K is characterized by a cusp in the field range of 0 to ±1 T. Beyond this field, it is nearly linear in the magnetic field. This cusplike feature of MR disappears above ≈20 K. A similar feature is also seen in the 2 K data of the 150 °C deposited film, although it is confined to a narrow range of field. This cusp in MR can be understood in the framework of the WAL effect in two-dimensional (2D) disordered films. It arises because the out-of-plane magnetic field suppresses coherent backscattering of electrons due to weak localization. The absence of any cusp in the MR data of 200 °C grown film is consistent with the absence of weak localization in this sample. The WAL effect has been seen in the MBE grown Sb_2Te_3 epitaxial film at 3.4 K for a very narrow magnetic field range (≈ ±0.1 T) [27]. We fit the magnetoconductivity data to the well-known Hikami-Larkin-Nagaoka (HLN) model [56] for the WAL effect, where the change in electrical conductivity is expressed as

$$\Delta\sigma = \frac{\alpha e^2}{2\pi^2\hbar}\left[\Psi\left(\frac{1}{2}+\frac{\hbar}{4el_\phi^2B}\right)-\ln\left(\frac{\hbar}{4el_\phi^2B}\right)\right]. \quad (4)$$

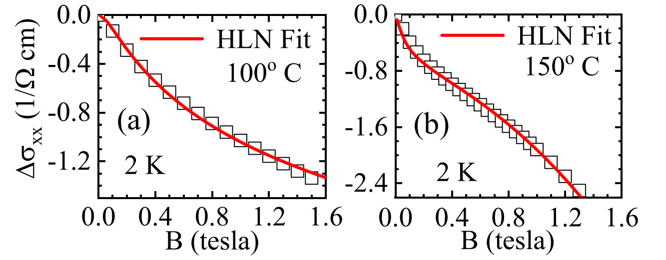

FIG. 6. Magnetoconductivity as a function of magnetic field at 2 K for (a) 100 °C and (b) 150 °C grown samples. The corresponding Hikami-Larkin-Nagaoka (HLN) fits are shown by red curves.

Here, Ψ is a digamma function, l_ϕ the phase coherence length of charge carriers, and the parameter α allows us to estimate the number of conduction channels participating in transport. The value of α is $-\frac{1}{2}$ per conduction channel in 2D electron systems [57,58]. We calculate the magnetoconductivity $[\Delta\sigma_{xx} = \sigma_{xx}(B) - \sigma_{xx}(0)]$ from the resistivity data using the expression $\sigma_{xx} = \rho_{xx}/(\rho_{xx}^2 + \rho_{xy}^2)$, where $\sigma_{xx}(0)$ and $\sigma_{xx}(B)$ are the conductivities at zero field and in magnetic field B, respectively. The $\Delta\sigma_{xx}$ data measured at 2 K for 100 and 150 °C grown samples fit well to the HLN equation in the field range of $-1.5 \leqslant B \leqslant 1.5$ T, as shown in Fig. 6. The fitting yields $\alpha \approx -0.06$ and $l_\phi \approx 64$ nm for the 100 °C grown film. Similarly, the extracted values for the 150 °C grown film are $\alpha \approx -0.02$ and $l_\phi \approx 245$ nm. It is instructive to compare these numbers with the data on Sb_2Te_3 samples in different forms. In monocrystalline nanowires, the prefactor $\alpha \approx -\frac{1}{2}$, indicating surface-state dominated transport [59], whereas for epitaxial films grown using MBE, $\alpha \approx -1$, suggesting a clean surface and interface of the film, which contribute equally to transport [27]. The significantly smaller magnitude of α seen in the present case suggests that the transport is dominantly governed by the bulk states. A similar behavior is seen in textured films of $Bi_{85}Sb_{15}$ [60] and Bi_2Te_3 [61,62]. Since electrical conduction in the films grown at 25 °C follows the VRH mechanism [shown in Figs. 2(b) and 2(c)], we apply the SE approach to analyze the MR data as well. The magnetic-field-dependent resistivity in this case is expressed as [35,50]

$$\ln\left[\frac{\rho(B)}{\rho(0)}\right] = K_sB^2, \quad \text{for } B < B_C, \quad (5a)$$

and

$$\ln\left[\frac{\rho(B)}{\rho(0)}\right] = f(B), \quad \text{for } B > B_C, \quad (5b)$$

where B_C defines the critical field which separates the two regimes of behavior expressed by Eqs. (5a) and (5b). For ES-type VRH with $p = 2$ [see Eq. (1)], K_s and $f(B)$ are

$$K_s = \frac{t\left[e^2a_B^4\right]\left[\frac{T_0}{T}\right]^{3/2}}{c^2\hbar^2}, \quad (6a)$$

and,

$$f(B) = \left[\frac{T_0}{T}\right]^{3/5}, \quad (6b)$$

where $T_0(B) = \beta e^2/\kappa a^*$ and $a^* = [\hbar\frac{a_B}{eB}]^{1/3}$.

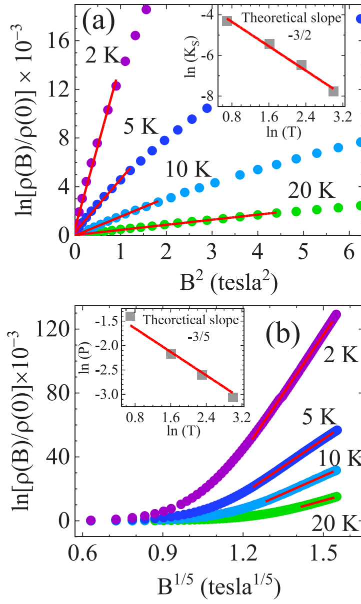

FIG. 7. Magnetoresistance (MR) as a function of (a) B^2 and (b) $B^{1/5}$ at the low-temperature range for the room-temperature grown sample. The insets of both panels represent natural log of the slopes (calculated from the linear fit of the MR data) vs natural log of the temperature. The ln(K_s) vs ln(T) and ln(P) vs ln(T) data support the theoretical predictions of $K_s \propto T^{-3/2}$ and $P \propto T^{-3/5}$, respectively.

The parameters are defined as a_B is the Bohr radius, β is a numerical constant, κ is dielectric constant, e is electronic charge, $\hbar$ is the Dirac constant, and c is the velocity of light. Figure 7(a) shows the $\rho(B)$ data of the RT sample at $T \leqslant 20$ K plotted following Eq. (5a). The quadratic field dependence of $\rho(B)/\rho_0$ at low fields suggests that the electrical conduction due to VRH is of the SE type [34,35]. The deviation of MR from the B^2 dependence in Fig 7(a) marks the critical field B_C. The MR at high field is better expressed by Eq. (5b), as shown in Fig. 7(b). We also realize that the slopes of K_s and $f(B)$ calculated from Eqs. (6a) and (6b) are proportional to $T^{-3/2}$ and $T^{-3/5}$, respectively. The insets of Figs. 7(a) and 7(b) show the ln(K_s)vs ln(T) and ln(P)vs ln(T), respectively. We observe perfect fits to the theoretically predicted slopes of $-\frac{3}{2}$ and $-\frac{3}{5}$ for $B < B_C$ and $B > B_C$, respectively.

D. Anisotropic backscattering of charge carriers—AMR and PHE

The spin-orbit-interaction-driven backscattering of charge carriers results in an anisotropic charge transport as the angle ϕ between the current density and magnetic field vectors laying on the plane of the film is changed from 0 to 2π. Such angular dependence of ρ_{xx} and ρ_{xy} allows the extraction of AMR and PHE in magnetically ordered metals [63]. In recent years, the anisotropic backscattering of charge carriers has been seen in nonmagnetic materials as well where the band topology dominates electronic transport [60–62,64–67]. We have measured the AMR and PHE of Sb_2Te_3 films in a geometry where the transport current $\mathbf{J}_x$ flows along the length of the Hall bar, and the induced electric fields $\mathbf{E}_x$ and $\mathbf{E}_y$ are measured while the sample is rotated in the xy plane from 0 to 2π with respect to the direction of a coplanar magnetic field ($\mathbf{B}$). The angle ϕ between $\mathbf{J}_x$ and $\mathbf{B}$ is zero when these two vectors are parallel to each other. In metallic ferromagnets, the longitudinal (ρ_{xx}) and transverse (ρ_{xy}) components of the resistivity tensor in this geometry can be expressed as [60,63,64]

$$\rho_{xx} = \rho_{\perp} + \Delta\rho\cos^2\phi, \tag{7a}$$

and

$$\rho_{xy} = \mp\Delta\rho \sin\phi\cos\phi, \tag{7b}$$

where $\Delta\rho = \rho_{\parallel} - \rho_{\perp}$, and $\rho_{\perp}$ and $\rho_{\parallel}$ correspond to the values of ρ_{xx} for B perpendicular and B parallel to $\mathbf{J}_x$, respectively. Since the ρ_{xx} and ρ_{xy} measurements are contaminated by erroneous misalignment of the plane of rotation and film plane, which results in a nonzero out-of-plane component of the magnetic field, we collect ρ_{xx} and ρ_{xy} data for both positive and negative magnetic field and then symmetrize the measured values to eliminate the antisymmetric (Hall) contribution. Also, even after symmetrization of ρ_{xy} [$= \{\rho_{xy}(+H) + \rho_{xy}(-H)\}/2$], a zero-field misalignment voltage across the Hall contacts will add to the PHE resistivity (ρ_{xy}). However, if the true PHE is significantly larger than the magnetic-field-induced change in this constant voltage, it can be subtracted from the measured ρ_{xy}. Figure 8 summarizes the results of AMR and PHE measurements on the 100 °C grown sample. The variation of the longitudinal resistivity as a function of angle ϕ (ρ_{xx}^{ϕ}) with respect to its value at $\phi = 90°$ ($\rho_{xx}^{\perp}$) is shown in Figs. 8(a) and 8(b) at a fixed field (9 T) and at fixed temperature (2 K) with T and B as parameters, respectively. Following Eqs. 7(a) and 7(b), the peak value of AMR ($\Delta\rho$) is negative in both cases. The inequality ($\rho_{\perp} > \rho_{\parallel}$) seen here is consistent with the observations made on other topological materials. The temperature and field dependence of peak AMR are summarized in Figs. 8(e) and 8(f). The constant field (9 T) AMR amplitude at 300 K is ≈−102 nΩ m. and it decreases with temperature to reach a value ≈−86 nΩ m at ≈200 K. A further drop in temperature results in enhanced AMR until an inflexion point is reached at ≈20 K. In the WAL regime of $T < 20$ K, we note a drop in AMR. The critical temperatures where the behavior of AMR changes are nearly the same as the temperatures where the slopes of carrier concentration and Hall mobility data shown in Fig. 3(f) change. The most striking result of this paper is presented in Fig. 8(f), which shows the field dependence of $\Delta\rho_{xx}$ at 2 K. It is negative ($\rho_{\perp} > \rho_{\parallel}$), nonsaturating up to the maximum field, and follows a B^2 field dependence. In Figs. 8(g) and 8(h), we summarize the behavior of the PHE (ρ_{xy}^{ϕ} with in-plane magnetic field). The oscillatory behavior of the PHE on variation of ϕ, with a period of π and the peak-to-peak amplitude nearly the same as $\rho_{xx}^{\perp} - \rho_{xx}^{\parallel}$, is consistent with Eqs. (7a) and (7b). Similarly, the temperature and field dependencies of the PHE amplitude are nearly the same as that of AMR, as expected from Eq. (7). The PHE amplitude at 300 K is ≈−73 nΩ m, which is more than an order of magnitude larger than in Bi_2Te_3 [61,62].

The AMR and PHE in magnetic alloys originate by virtue of the *s-d* scattering near the Fermi energy. However, these effects are not limited to only magnetic systems and recently have been realized in nonmagnetic TIs and Dirac/Weyl

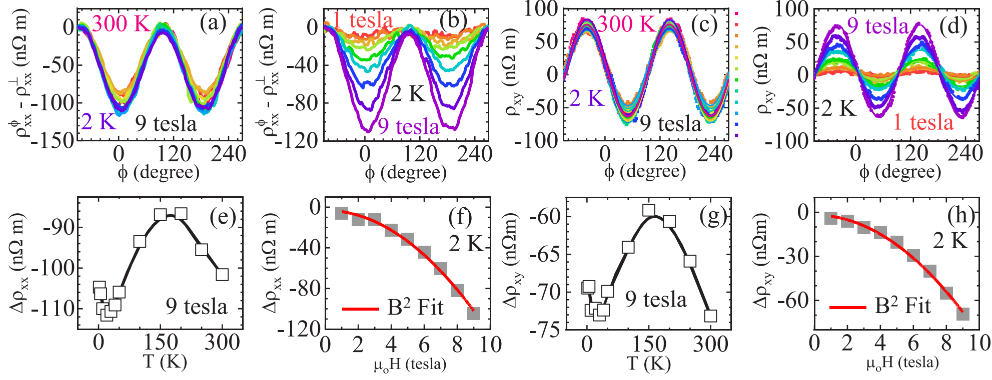

FIG. 8. Anisotropic magnetoresistance (AMR) and planar Hall effect (PHE) measurements performed on 100 °C grown Sb_2Te_3 sample: (a) $\rho_{xx}^{\phi} - \rho_{xx}^{\perp}$ vs ϕ in 9 T field at various temperatures ranging from 2 to 300 K, (b) $\rho_{xx}^{\phi} - \rho_{xx}^{\perp}$ vs ϕ measured at 2 K for several values of magnetic field, (c) ρ_{xy} vs ϕ in 9 T measured at several temperatures, and (d) the ρ_{xy} data at 2 K at constant field ranging from 1 to 9 T. (e) and (f) show the variation of the peak amplitude of AMR [Eq. (4a)] as a function of temperature at 9 T and as a function of field at 2 K, respectively. (g) and (h) show the variation of PHE amplitude at 9 T as a function of temperature and at 2 K measured at several fields, respectively.

semimetals [65–70]. Figure 9 displays a comparison of the PHE magnitude $|\Delta\rho_{xy}|$ for different material systems taken from the literature. The semimetals such as bismuth [71,72], GdPtBi [72,73], TaP [74], Cd_3As_2 [75], $ZrTe_2$ [76], VAl_3 [77], and $MoTe_2$ [78] possess very large ($>10^4$ nΩ m) PHE amplitude. Compared with these values, the PHE of the TI Bi_2Te_3 is rather low [61,62]. The PHE amplitudes of the epitaxial Sb_2Te_3 film reported here is an order of magnitude higher than the PHE of crystalline Bi_2Te_3 [61,62] and Weyl semimetal $NiTe_2$ [80]. However, the AMR and PHE amplitudes of 200 °C grown epitaxial Sb_2Te_3 are ≈ -9 and -11 nΩ m, respectively, which is ~6 times smaller than the 100 °C grown epitaxial Sb_2Te_3 but still larger than Bi_2Te_3 [61,62]. The AMR and PHE data for 200 °C grown epitaxial Sb_2Te_3

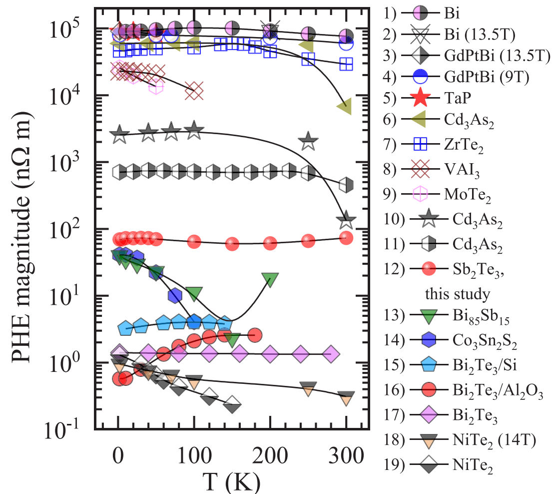

FIG. 9. Temperature-dependent planar Hall effect (PHE) magnitude $|\Delta\rho_{xy}|$ comparison of various materials from the literature with this paper. References: (1) bismuth [71], (2) bismuth (13.5 T) [72], (3) GdPtBi (13.5 T) [72], (4) GdPtBi (9 T) [73], (5) TaP [74], (6) Cd_3As_2 [75], (7) $ZrTe_2$ [76], (8) VAl_3 [77], (9) $MoTe_2$ [78], (10) Cd_3As_2 [75], (11) Cd_3As_2 [75], (12) this paper, (13) $Bi_{85}Sb_{15}$ [60], (14) $Co_3Sn_2S_2$ [79], (15) Bi_2Te_3/Al_2O_3 [62], (16) Bi_2Te_3/Si [62], (17) Bi_2Te_3 [61], (18) $NiTe_2$ (14 T) [80], and (19) $NiTe_2$ [80].

film measured at 300 K with the application of 9 T magnetic field are shown in Fig. S3 in the Supplemental Material [41]. The conduction in topologically protected surface states and a nontrivial band topology are the origins of AMR and PHE in these materials [64,68]. The PHE may also derive an anomalous contribution from hexagonal-wrapped 2D surface states in the TIs which is expected to have a $2\pi/3$ periodicity and B^3 field dependence [69,70]. We have used the approach described by Wang *et al.* [70] to extract the buried anomalous planar Hall effect (APHE) signal in the data of Figs. 8(c) and 8(d). The result of this analysis presented in Fig. S4 in the Supplemental Material [41] does not indicate a $2\pi/3$ periodicity and B^3 field dependence. In addition, the strong spin-orbit coupling in some of these heavy-element-based systems may also lead to anisotropic in-plane transport [60,61]. Several experiments and theories also highlight a magnetic-disorder-induced anisotropic backscattering contributing to the PHE of the TIs. An experimental observation of the PHE by Taskin *et al.* [64] in doped $Bi_{2-x}Sb_xTe_3$ is argued to be due to the spins of magnetic impurities in the system. Zheng *et al.* [67] proposed a microscopic mechanism to account for the observation of AMR and PHE in TIs. They suggest that the tilting of the Dirac cone by virtue of an in-plane applied field may lead to AMR, independent of the magnetic nature of the scatterers. The nontopological generation of the PHE in TIs or even in Weyl/Dirac semimetals can also be understood by this tilt-induced PHE theory [67].

The chiral anomaly has also been considered the origin of the PHE in Weyl/Dirac semimetals [72,79]. We explore this possibility in Fig. 10 by plotting the ρ_{xy} vs ρ_{xx} orbits generated from the data of Figs. 8(b) and 8(d) collected for different field values at 2 K. The criterion for the presence of the chiral anomaly is that all the orbits measured at different fields should be concentric [72,80,81]. Such plots have been seen for Na_3Bi and GdPtBi where the source of the PHE is chiral anomaly [72]. On the other hand, the systems such as Bi [72], $NiTe_2$ [80] and $TaSe_3$ [81], with no chiral anomaly show a shock-wave-type expansion, where the orbits expand strongly to the left, indicating that the higher mobility creates exaggerated skewing of the leftward expansion. The formation of a shock-wave pattern in the parametric plot

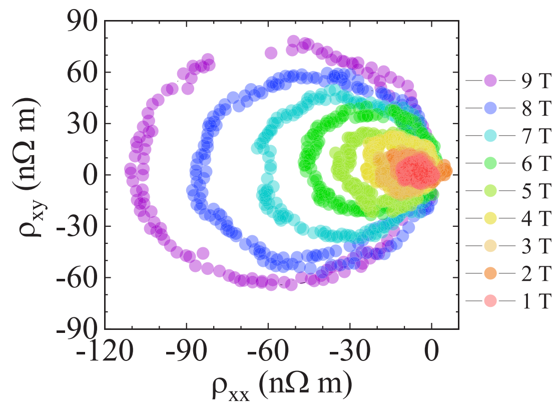

FIG. 10. The ρ_{xy} vs ρ_{xx} orbit plot for specified magnetic fields with angle θ parametrization, measured at 2 K. The shock-wave pattern formation as the orbits evolve suggests the absence of chiral anomaly.

indicates the absence of a chiral anomaly in these Sb_2Te_3 film.

The Sb_2Te_3 films investigated here are relatively thick with broader FWHM of the diffraction lines, suggesting deviation from ideal epitaxy. Also, the value of parameter α is -0.06, which is very low. It is likely that the topological surface states are not fully preserved [27,57–59]. Moreover, it is known that the bulk states contribute predominantly to AMR and PHE in thicker films of TIs [60–62]. This could be a reason for the generation of AMR and PHE in these Sb_2Te_3 epitaxial samples.

IV. CONCLUSIONS

In summary, the sesquichalcogenide Sb_2Te_3 is an important semimetal due to its thermoelectricity and its recently discovered band topology which puts it in the category of quantum materials. We have addressed the charge carrier transport and anisotropic backscattering of charge carriers in thin films of Sb_2Te_3 with different degrees of crystallographic order stabilized by controlling their growth temperature. While the RT grown films are an ensemble of nanocrystals dispersed in an amorphous host, the films grown at 100, 150, and 200 °C are epitaxial with FWHM of ω scans as narrow as 0.17 ° and 0.16 °, respectively. Charge transport in the disordered films has prominent signatures of the SE VRH with the characteristic localization length and Coulomb gap of ≈12 nm and 0.3 meV, respectively. The majority charge carriers in epitaxial films are holes with a density of $\sim 10^{19}$ cm^{-3} and Hall mobility of $\sim 10^2$ $cm^2\,V^{-1}\,s^{-1}$, displaying no significant change in the temperature range of 2–300 K. The OMR of the epitaxial films is positive, nonsaturating until the maximum field of 9 T, and follows Kohler's rule if the temperature dependence of the carrier density is accounted for. WAL is a dominant feature of transport at $T \leqslant 20$ K in epitaxial film grown at $T \leqslant 150$ °C, whereas Te vacancies in samples grown at higher temperatures suppress it. The samples show robust anisotropic back scattering of charge carriers in a magnetic field. The measured negative PHE amplitude of ∼73 nΩ m is an order of magnitude larger than the PHE of Bi_2Te_3 films. We believe that these AMR and PHE results for epitaxial Sb_2Te_3 films would be valuable for the development of sensors and for understanding electronic transport in similar topological materials.

ACKNOWLEDGMENTS

This paper is supported by the United States Department of Defense, Center of Excellence for Advanced Electro-Photonics with 2D Materials at Morgan State University, Grant No. W911NF2120213. The transmission electron microscope used here is funded by the National Institute of General Medical Sciences of the National Institutes of Health under Award No. UL1GM118973.

[1] D. K. Ko, Y. Kang, and C. B. Murray, Enhanced thermopower via carrier energy filtering in solution-processable Pt-Sb_2Te_3 nanocomposites, Nano Lett. **11**, 2841 (2011).
[2] K. Wang, D. Graf, and C. Petrovic, Large magnetothermopower and Fermi surface reconstruction in Sb_2Te_2Se, Phys. Rev. B **89**, 125202 (2014).
[3] A. Ahmed and S. Han, Optimizing the structural, electrical and thermoelectric properties of antimony telluride thin films deposited on aluminum nitride-coated stainless steel foil, Sci. Rep. **10**, 6978 (2020).
[4] Z. Ju, C. Crawford, J. Adamczyk, E. S. Toberer, and S. M. Kauzlarich, Study of the thermoelectric properties of Bi_2Te_3/Sb_2Te_3 core-shell heterojunction nanostructures, ACS Appl. Mater. Interfaces **14**, 24886 (2022).
[5] A. M. Adam, E. M. Elsehly, M. Ataalla, A. El-Khouly, A. Nafady, and A. K. Diab, Preparation and thermoelectric power properties of highly doped p-type Sb_2Te_3 thin films, Physica E **127**, 114505 (2021).
[6] Y. Kim, A. DiVenere, G. K. L. Wong, J. B. Ketterson, S. Cho, and J. R. Meyer, Structural and thermoelectric transport properties of Sb_2Te_3 thin films grown by molecular beam epitaxy, J. Appl. Phys. **91**, 715 (2002).
[7] J. Wang, C. Zhou, Y. Yu, Y. Zhou, L. Lu, B. Ge, Y. Cheng, C.-L. Jia, R. Mazzarello, Z. Shi *et al.*, Enhancing thermoelectric performance of Sb_2Te_3 through swapped bilayer defects, Nano Energy **79**, 105484 (2021).
[8] T. Q. Kimberly, K. M. Ciesielski, X. Qi, E. S. Toberer, and S. M. Kauzlarich, High thermoelectric performance in 2D Sb_2Te_3 and Bi_2Te_3 nanoplate composites enabled by energy carrier filtering and low thermal conductivity, ACS Appl. Electron. Mater. (2023).
[9] P. A. Finn, C. Asker, K. Wan, E. Bilotti, O. Fenwick, and C. B. Nielsen, Thermoelectric materials: Current status and future challenges, Front. Electron. Mater. **1**, 677845 (2021).
[10] D. Das, K. Malik, A. K. Deb, S. Dhara, S. Bandyopadhyay, and A. Banerjee, Defect induced structural and thermoelectric properties of Sb_2Te_3 alloy, J. Appl. Phys. **118**, 045102 (2015).

[11] P. Dutta, D. Bhoi, A. Midya, N. Khan, P. Mandal, S. Shanmukharao Samatham, and V. Ganesan, Anomalous thermal expansion of Sb_2Te_3 topological insulator, Appl. Phys. Lett. **100**, 251912 (2012).

[12] Z. Zeng, T. A. Morgan, D. Fan, C. Li, Y. Hirono, X. Hu, Y. Zhao, J. S. Lee, J. Wang, Z. M. Wang *et al.*, Molecular beam epitaxial growth of Bi_2Te_3 and Sb_2Te_3 topological insulators on GaAs (111) substrates: A potential route to fabricate topological insulator *p-n* junction, AIP Adv. **3**, 072112 (2013).

[13] V. A. Kulbachinskii, Z. M. Dashevskii, M. Inoue, M. Sasaki, H. Negishi, W. X. Gao, P. Lostak, J. Horak, and A. De Visser, Valence-band changes in $Sb_{2-x}In_xTe_3$ and $Sb_2Te_{3-y}Se_y$ by transport and Shubnikov–de Haas effect measurements, Phys. Rev. B **52**, 10915 (1995).

[14] H. Zhang, C.-X. Liu, X.-L. Qi, X. Dai, Z. Fang, and S.-C. Zhang, Topological insulators in Bi_2Se_3, Bi_2Te_3 and Sb_2Te_3 with a single Dirac cone on the surface, Nat. Phys. **5**, 438 (2009).

[15] Y. L. Chen, J. G. Analytis, J.-H. Chu, Z. K. Liu, S.-K. Mo, X. L. Qi, H. J. Zhang, D. H. Lu, X. Dai, Z. Fang *et al.*, Experimental realization of a three-dimensional topological insulator, Bi_2Te_3, Science **325**, 178 (2009).

[16] S. Urazhdin, D. Bilc, S. D. Mahanti, S. H. Tessmer, T. Kyratsi, and M. G. Kanatzidis, Surface effects in layered semiconductors Bi_2Se_3 and Bi_2Te_3, Phys. Rev. B **69**, 085313 (2004).

[17] Y. Zhang, K. He, C.-Z. Chang, C.-L. Song, L.-L. Wang, X. Chen, J.-F. Jia, Z. Fang, X. Dai, W.-Y. Shan *et al.*, Crossover of the three-dimensional topological insulator Bi_2Se_3 to the two-dimensional limit, Nat. Phys. **6**, 584 (2010).

[18] H. E. Lund, K. Volckaert, P. Majchrzak, A. J. H. Jones, M. Bianchi, M. Bremholm, and P. Hofmann, Bulk band structure of Sb_2Te_3 determined by angle-resolved photoemission spectroscopy, Phys. Chem. Chem. Phys. **23**, 26401 (2021).

[19] K. Kuroda, J. Reimann, K. A. Kokh, O. E. Tereshchenko, A. Kimura, J. Güdde, and U. Höfer, Ultrafast energy- and momentum-resolved surface Dirac photocurrents in the topological insulator Sb_2Te_3, Phys. Rev. B **95**, 081103(R) (2017).

[20] L. Locatelli, A. Kumar, P. Tsipas, A. Dimoulas, E. Longo, and R. Mantovan, Magnetotransport and ARPES studies of the topological insulators Sb_2Te_3 and Bi_2Te_3 grown by MOCVD on large-area Si substrates, Sci. Rep. **12**, 3891 (2022).

[21] G. Wang, X. Zhu, J. Wen, X. Chen, K. He, L. Wang, X. Ma, Y. Liu, X. Dai, Z. Fang *et al.*, Atomically smooth ultrathin films of topological insulator Sb_2Te_3, Nano Res. **3**, 874 (2010).

[22] Z. W. Sun, K. W. Cheng, S. W. Lin, V. K. Ranganayakulu, Y. Y. Chen, S. J. Chiu, T. W. Lee, and A. T. Wu, Stoichiometric effect of Sb_2Te_3 thin film on thermoelectric property, ACS Appl. Energy Mater. **5**, 7026 (2022).

[23] V. D. Das and N. Soundararajan, Thermoelectric power and electrical resistivity of crystalline antimony telluride (Sb_2Te_3) thin films: Temperature and size effects, J. Appl. Phys. **65**, 2332 (1989).

[24] A. Singh, V. K. Gangwar, P. Shahi, D. Pal, R. Singh, S. Kumar, S. Singh, S. K. Gupta, S. Kumar, J. Cheng *et al.*, Anomalous and topological Hall effect in Cu doped Sb_2Te_3 topological insulator, Appl. Phys. Lett. **117**, 092403 (2020).

[25] Y.-C. Huang, P. C. Lee, C. H. Chien, F. Y. Chiu, Y. Y. Chen, and S. R. Harutyunyan, Magnetotransport properties of Sb_2Te_3 nanoflake, Physica B **452**, 108 (2014).

[26] C. Weyrich, T. Merzenich, J. Kampmeier, I. E. Batov, G. Mussler, J. Schubert, D. Grützmacher, and T. Schäpers, Magnetoresistance oscillations in MBE-grown Sb_2Te_3 thin films, Appl. Phys. Lett. **110**, 092104 (2017).

[27] Y. Takagaki, A. Giussani, K. Perumal, R. Calarco, and K. J. Friedland, Robust topological surface states in Sb_2Te_3 layers as seen from the weak antilocalization effect, Phys. Rev. B **86**, 125137 (2012).

[28] X. Zhang, Z. Zeng, C. Shen, Z. Zhang, Z. Wang, C. Lin, and Z. Hu, Investigation on the electrical transport properties of highly (00l)-textured Sb_2Te_3 films deposited by molecular beam epitaxy, J. Appl. Phys. **115**, 024307 (2014).

[29] B. Fang, Z. Zeng, X. Yan, and Z. Hu, Effects of annealing on thermoelectric properties of Sb_2Te_3 thin films prepared by radio frequency magnetron sputtering, J. Mater. Sci. Mater. Electron. **24**, 1105 (2013).

[30] Y. Saito, P. Fons, L. Bolotov, N. Miyata, A. V. Kolobov, and J. Tominaga, A two-step process for growth of highly oriented Sb_2Te_3 using sputtering, AIP Adv. **6**, 045220 (2016).

[31] M. Tan, Y. Deng, Y. Wang, B. Luo, L. Liang, and L. Cao, Fabrication of highly (00l)-textured Sb_2Te_3 film and corresponding thermoelectric device with enhanced performance, J. Electron. Mater. **41**, 3031 (2012).

[32] G. Bendt, S. Zastrow, K. Nielsch, P. S. Mandal, J. Sánchez-Barriga, O. Rader, and S. Schulz, Deposition of topological insulator Sb_2Te_3 films by an MOCVD process, J. Mater. Chem. A Mater. **2**, 8215 (2014).

[33] S. Nandy, G. Sharma, A. Taraphder, and S. Tewari, Chiral anomaly as the origin of the planar Hall effect in Weyl semimetals, Phys. Rev. Lett. **119**, 176804 (2017).

[34] O. Ivanov and M. Yaprintsev, Variable-range hopping conductivity in Lu-doped Bi_2Te_3, Solid State Sci. **76**, 111 (2018).

[35] S. M. Wasim, L. Essaleh, G. Marín, C. Rincón, S. Amhil, and J. Galibert, Efros-Shklovskii type variable range hopping conduction and magnetoresistance in *p*-type $CuGa_3Te_5$, Superlattices Microstruct. **107**, 285 (2017).

[36] M. Pollak and B. Shklovskii, *Hopping Transport in Solids* (Elsevier Science, Amsterdam, 1991), Vol. 28.

[37] D. Nandi, B. Skinner, G. H. Lee, K.-F. Huang, K. Shain, C.-Z. Chang, Y. Ou, S.-P. Lee, J. Ward, J. S. Moodera *et al.*, Signatures of long-range-correlated disorder in the magnetotransport of ultrathin topological insulators, Phys. Rev. B **98**, 214203 (2018).

[38] J. Zhang and B. I. Shklovskii, Density of states and conductivity of a granular metal or an array of quantum dots, Phys. Rev. B **70**, 115317 (2004).

[39] J. Xu, F. Han, T.-T. Wang, L. R. Thoutam, S. E. Pate, M. Li, X. Zhang, Y.-L. Wang, R. Fotovat, U. Welp *et al.*, Extended Kohler's rule of magnetoresistance, Phys. Rev. X **11**, 041029 (2021).

[40] Z. Liao, M. Brahlek, J. M. Ok, L. Nuckols, Y. Sharma, Q. Lu, Y. Zhang, and H. N. Lee, Pulsed-laser epitaxy of topological insulator Bi_2Te_3 thin films, APL Mater. **7**, 041101 (2019).

[41] See Supplemental Material at http://link.aps.org/supplemental/10.1103/PhysRevB.109.075421 for TEM micrograph of RT grown Sb_2Te_3 film, extended Kohler's rule and planar Hall effect of 200 °C sample. The micrograph suggests a highly disordered structure consisting of nanosized crystallites imbedded in an amorphous matrix. Selected area electron diffraction

pattern showing weak spots along with the concentric rings, suggesting poor crystallization. The extended Kohler's for 150 and 200 °C samples shows significant convergence compared to conventional Kohler's rule. The AMR and PHE amplitudes of 200 °C grown sample measured at 300 K in presence of 9 tesla field come out to be ~ -9 and -11 nΩ m, respectively. The extracted anomalous planar Hall effect for 100 °C sample does not show any $2\pi/3$ periodicity.
[42] S. M. Huang, K. J. Chen, Y. J. Yan, S. H. Yu, and M. Chou, The thickness-induced magneto-transport and optic properties enhancement in Sb_2Te_3 flakes, Sci. Rep. **8**, 16690 (2018).
[43] N. Mott, *Metal-Insulator Transitions* (Taylor & Francis, London, 2004).
[44] D. Joung and S. I. Khondaker, Efros-Shklovskii variable-range hopping in reduced graphene oxide sheets of varying carbon sp^2 fraction, Phys. Rev. B **86**, 235423 (2012).
[45] K. Ulutas, Ş. Yakut, and D. Deger, Dielectric polarization in Sb_2Te_3 thin films, IOP Conf. Ser. Mater. Sci. Eng. **15**, 012038 (2010).
[46] K. G. Lisunov, E. Arushanov, G. A. Thomas, E. Bucher, and J. H. Schön, Variable-range hopping conductivity and magnetoresistance in n-$CuGaSe_2$, J. Appl. Phys. **88**, 4128 (2000).
[47] A. L. Efros, Coulomb gap in disordered systems, J. Phys. C Solid State Phys. **9**, 2021 (1976).
[48] Y. Huang, Y. He, B. Skinner, and B. I. Shklovskii, Conductivity of two-dimensional narrow gap semiconductors subjected to strong Coulomb disorder, Phys. Rev. B **105**, 054206 (2022).
[49] A. M. Glukhov, N. Ya. Fogel, and A. A. Shablo, Coulombic gap and hopping conduction in granulated metal-semiconductor films, Sov. Phys. Solid State **28**, 1043 (1986).
[50] B. I. Shklovskii and A. L. Efros, *Electronic Properties of Doped Semiconductors* (Springer, Berlin, 1984), Vol. 45.
[51] J. H. Schön, E. Arushanov, N. Fabre, and E. Bucher, Transport properties of n-type $CuGaSe_2$, Sol. Energy Mater. Sol. Cells **61**, 417 (2000).
[52] T. Holstein, Hall effect in impurity conduction, Phys. Rev. **124**, 1329 (1961).
[53] A. Avdonin, P. Skupiński, and K. Grasza, Hall effect in hopping regime, Physica B **483**, 13 (2016).
[54] Y. L. Wang, L. R. Thoutam, Z. L. Xiao, J. Hu, S. Das, Z. Q. Mao, J. Wei, R. Divan, A. Luican-Mayer, G. W. Crabtree, and W. K. Kwok, Origin of the turn-on temperature behavior in WTe_2, Phys. Rev. B **92**, 180402(R) (2015).
[55] Q. L. Pei, W. J. Meng, X. Luo, H. Y. Lv, F. C. Chen, W. J. Lu, Y. Y. Han, P. Tong, W. H. Song, Y. B. Hou *et al.*, Origin of the turn-on phenomenon in T_d-$MoTe_2$, Phys. Rev. B **96**, 075132 (2017).
[56] S. Hikami, A. I. Larkin, and Y. O. Nagaoka, Spin-orbit interaction and magnetoresistance in the two dimensional random system, Prog. Theor. Phys. **63**, 707 (1980).
[57] J. Chen, H. J. Qin, F. Yang, J. Liu, T. Guan, F. M. Qu, G. H. Zhang, J. R. Shi, X. C. Xie, C. L. Yang *et al.*, Gate-voltage control of chemical potential and weak antilocalization in Bi_2Se_3, Phys. Rev. Lett. **105**, 176602 (2010).
[58] H. T. He, G. Wang, T. Zhang, I. K. Sou, G. K. L. Wong, J. N. Wang, H. Z. Lu, S. Q. Shen, and F. C. Zhang, Impurity effect on weak antilocalization in the topological insulator Bi_2Te_3, Phys. Rev. Lett. **106**, 166805 (2011).
[59] B. Hamdou, J. Gooth, A. Dorn, E. Pippel, and K. Nielsch, Aharonov-Bohm oscillations and weak Antilocalization in topological insulator Sb_2Te_3 nanowires, Appl. Phys. Lett. **102**, 223110 (2013).
[60] R. C. Budhani, J. S. Higgins, D. McAlmont, and J. Paglione, Planar Hall effect in c-axis textured films of $Bi_{85}Sb_{15}$ topological insulator, AIP Adv **11**, 055020 (2021).
[61] R. Nepal, V. Sharma, L. Pogue, N. Drichko, and R. C. Budhani, Disorder driven variations in magnetoresistance and planar Hall effect in Bi_2Te_3 thin films, Thin. Solid. Films **761**, 139520 (2022).
[62] A. Bhardwaj, S. Prasad P., K. V. Raman, and D. Suri, Observation of planar Hall effect in topological insulator—Bi_2Te_3, Appl. Phys. Lett. **118**, 241901 (2021).
[63] I. A. Campbell and A. Fert, The spontaneous resistivity anisotropy in Ni-based alloys, J. Phys. C: Solid State Phys. **3**, S95 (1970).
[64] A. A. Taskin, H. F. Legg, F. Yang, S. Sasaki, Y. Kanai, K. Matsumoto, A. Rosch, and Y. Ando, Planar Hall effect from the surface of topological insulators, Nat. Commun. **8**, 1340 (2017).
[65] A. A. Burkov, Giant planar Hall effect in topological metals, Phys. Rev. B **96**, 041110(R) (2017).
[66] S. Nandy, A. Taraphder, and S. Tewari, Berry phase theory of planar Hall effect in topological insulators, Sci. Rep. **8**, 14983 (2018).
[67] S. H. Zheng, H. J. Duan, J. K. Wang, J. Y. Li, M. X. Deng, and R. Q. Wang, Origin of planar Hall effect on the surface of topological insulators: Tilt of Dirac cone by an in-plane magnetic field, Phys. Rev. B **101**, 041408(R) (2020).
[68] B. Wu, X. C. Pan, W. Wu, F. Fei, B. Chen, Q. Liu, H. Bu, L. Cao, F. Song, and B. Wang, Oscillating planar Hall response in bulk crystal of topological insulator Sn doped $Bi_{1.1}Sb_{0.9}Te_2S$, Appl. Phys. Lett. **113**, 011902 (2018).
[69] R. S. Akzyanov and A. L. Rakhmanov, Surface charge conductivity of a topological insulator in a magnetic field: The effect of hexagonal warping, Phys. Rev. B **97**, 075421 (2018).
[70] C. M. Wang, Z. Z. Du, H.-Z. Lu, and X. C. Xie, Absence of the anomalous Hall effect in planar Hall experiments, Phys. Rev. B **108**, L121301 (2023).
[71] S. Y. Yang, K. Chang, and S. S. P. Parkin, Large planar Hall effect in bismuth thin films, Phys. Rev. Res. **2**, 022029(R) (2020).
[72] S. Liang, J. Lin, S. Kushwaha, J. Xing, N. Ni, R. J. Cava, and N. P. Ong, Experimental tests of the chiral anomaly magnetoresistance in the Dirac-Weyl semimetals Na_3Bi and GdPtBi, Phys. Rev. X **8**, 031002 (2018).
[73] N. Kumar, S. N. Guin, C. Felser, and C. Shekhar, Planar Hall effect in the Weyl semimetal GdPtBi, Phys. Rev. B **98**, 041103(R) (2018).
[74] J. Yang, W. L. Zhen, D. D. Liang, Y. J. Wang, X. Yan, S. R. Weng, J. R. Wang, W. Tong, L. Pi, W. K. Zhu *et al.*, Current jetting distorted planar Hall effect in a Weyl semimetal with ultrahigh mobility, Phys. Rev. Mater. **3**, 014201 (2019).
[75] M. Wu, G. Zheng, W. Chu, Y. Liu, W. Gao, H. Zhang, J. Lu, Y. Han, J. Zhou, W. Ning *et al.*, Probing the chiral anomaly by planar Hall effect in Dirac semimetal Cd_3As_2 nanoplates, Phys. Rev. B **98**, 161110(R) (2018).
[76] P. Li, C. H. Zhang, J. W. Zhang, Y. Wen, and X. X. Zhang, Giant planar Hall effect in the Dirac semimetal $ZrTe_{5-\delta}$, Phys. Rev. B **98**, 121108 (2018).

[77] R. Singha, S. Roy, A. Pariari, B. Satpati, and P. Mandal, Planar Hall effect in the type-II Dirac semimetal VAl_3, Phys. Rev. B **98**, 081103 (2018).

[78] D. D. Liang, Y. J. Wang, W. L. Zhen, J. Yang, S. R. Weng, X. Yan, Y. Y. Han, W. Tong, W. K. Zhu, L. Pi *et al.*, Origin of planar Hall effect in type-II Weyl semimetal $MoTe_2$, AIP Adv. **9**, 055015 (2019).

[79] S. Y. Yang, J. Noky, J. Gayles, F. K. Dejene, Y. Sun, M. Dörr, Y. Skourski, C. Felser, M. N. Ali, E. Liu *et al.*, Field-modulated anomalous Hall conductivity and planar Hall effect in $Co_3Sn_2S_2$ nanoflakes, Nano Lett. **20**, 7860 (2020).

[80] Q. Liu, F. Fei, B. Chen, X. Bo, B. Wei, S. Zhang, M. Zhang, F. Xie, M. Naveed, X. Wan *et al.*, Nontopological origin of the planar Hall effect in the type-II Dirac semimetal $NiTe_2$, Phys. Rev. B **99**, 155119 (2019).

[81] X. C. Yang, X. Luo, J. J. Gao, Z. Z. Jiang, W. Wang, T. Y. Wang, J. G. Si, C. Y. Xi, W. H. Song, and Y. P. Sun, Planar Hall effect in the quasi-one-dimensional topological superconductor $TaSe_3$, Phys. Rev. B **104**, 155106 (2021).